J. Fluid Mech. (1974), *vol.* 62, *part* 1, *pp.* 115–143
Printed in Great Britain

Measurements of the nearly isotropic turbulence behind a uniform jet grid

By MOHAMED GAD-EL-HAK† AND STANLEY CORRSIN
Department of Mechanics and Materials Science, The Johns Hopkins University

(Received 18 May 1973)

Wind-tunnel turbulence behind a parallel-rod grid with jets evenly distributed along each rod is nearly isotropic. Homogeneity improvement over prior related experiments was attained by the use of controllable nozzles. Compared with the 'passive' case, the downwind-jet 'active' grid has a smaller static pressure drop across it and gives a smaller turbulence level at a prescribed distance from it, while the upwind-jet grid gives a larger static pressure drop and larger turbulence level. 'Counterflow injection' generates larger turbulence energy and larger scales, both events being evidently associated with instability of the jet system. This behaviour is much like that commonly observed behind passive grids of higher solidities.

If the turbulent kinetic energy is approximated as an inverse power law in distance, the (positive) exponent decreases with increasing (downwind or upwind) jet strength, corresponding to slower absolute decay rates. No peculiar decay behaviour occurs when the jet grid is 'self-propelled' (zero net average force), or when the static pressure drop across it is zero.

The injection does not change the general behaviour of the energy spectra, although the absolute spectra change inasmuch as the turbulence kinetic energy changes.

CONTENTS

† Present address: Department of Aerospace Engineering, University of Southern California, Los Angeles, California 90007.

1. Introduction

The first reasonably successful attempt to generate nearly isotropic turbulence was that of Simmons & Salter (1934). They found that the turbulence at high Reynolds number far behind a periodic grid is a good laboratory realization of this simplest type of turbulence. The grid generates turbulence by acting simply as an obstacle to the flow; in that sense, it is 'passive'. Of course, in a general dynamic sense it is active indeed. For example, the boundary-layer separation lines move unsteadily. Almost all experiments on isotropic turbulence have been carried out using one form or another of the rigid, fixed (passive) grid. The resulting turbulence is rather insensitive to grid design parameters, except for solidity. Some results can be found in the papers of Stewart & Townsend (1951), Harris (1965), Comte-Bellot & Corrsin (1966) and Naudascher & Farell (1970).

A different type of turbulence generator is what might be called an 'active grid', i.e. one which in some sense has moving boundaries, or one which is capable of adding mean momentum to the fluid. Examples are grids which vibrate (e.g. Ling & Wan 1972), or grids which possess propellors or windmills, or grids which eject secondary fluid jets into the fluid stream.

Mathieu & Alcaraz (1965) were evidently the first to use a 'jet grid' as a means of generating intense turbulence with a reasonable degree of homogeneity. In their experiment and two succeeding ones (Guillon 1968; Charnay 1969) it was found that relatively high turbulence levels could be generated. Teunissen (1969) used a jet grid to drive his wind tunnel, and to generate turbulence with an arbitrary mean velocity profile. Luxenberg & Wiskind (1969) used a jet grid to study isotropic turbulence, specifically how the turbulence would change owing to injection. Liu, Greber & Wiskind (1971) tried to improve the homogeneity of the flow behind the jet grid.

A deficiency in those experiments was inhomogeneity of the flow field, even far behind the grid. This problem made it inappropriate to compare the results with passive-grid results, where the flow is nearly homogeneous and isotropic.

A good approximation to isotropy allows comparison with the basic simplified equations and theories of isotropic turbulence. In the present study, the jet grid had an individual throttle on each jet, to allow a reasonable degree of homogeneity far downstream.

A general objective was to study the effects of injection on various turbulence parameters. By variation of the relative 'strength' of the jets, the force on the grid was varied from average net drag to average net thrust; a particular jet strength yields zero net force on the grid. This suggests another question: is there any singular behaviour associated with this zero-force case, where the grid is acting as a self-propelled body? It is known that the wake of a single self-propelled body in unbounded flow decays at a rate different from that of a body with net drag or net thrust (e.g. Tennekes & Lumley 1972, p. 124).

Another objective was to investigate the possibility of generating a high turbulence level while maintaining a reasonable degree of homogeneity and isotropy.

2. Experimental equipment and procedure

The closed-circuit wind tunnel used in this experiment is described by Comte-Bellot & Corrsin (1966). The test section is about 10 m long, with a cross-section $1{\cdot}0 \times 1{\cdot}3$ m. The jet grid consists of 10 parallel brass pipes, whose centres are 10·2 cm apart (mesh size). Each rod is 137·2 cm long, with 3·8 cm and 3·4 cm outside and inside diameters, respectively. The geometric solidity† is 0·37. Each rod has 17 jets, 7·6 cm apart and with a 1 cm nominal (inside) diameter. The rate of flow from each jet is controlled by a needle valve. The secondary air is supplied to the grid through a 27×23 cm (cross-section) sheet-metal duct. Each rod is connected to the duct at both ends by flexible rubber gum tubing. The flow rate to each rod is throttled by squeezing each flexible tube with a clamp. The secondary-air blower‡ is directly driven by a 15 h.p., a.c. motor, through a gyrol fluid drive.§ The fluid drive provides smooth stepless speed regulation from 0 to 3600 r.p.m. The fan has a rated capacity of 2500 ft^3/min (1·18 m^3/s) at 50 cm of water head. Figure 1 (plate 1) shows the jet grid and the blower outside the wind tunnel, where the jets were adjusted to yield equal flow rates [see Gad-el-Hak (1972) for details of the adjustment procedure]. It is estimated that the difference between the mass flow rates from any two jets is no more than 3 %. Since the total jet flow rate was never more than 10 % of the total flow rate in the wind tunnel, this difference would probably cause less than 0·3 % inhomogeneity in the test-section mean flow.

Velocity fluctuations were measured with two Disa type 55D01 constant-temperature anemometers, in conjunction with two Disa type 55D10 linearizers. Overheat ratios of 0·7–0·8 and a linearized exponent setting of 2·2 were used, yielding a linear net calibration curve. The linearizer outputs were filtered by two Disa type 55D25 auxiliary units. Each is an amplifier with separately adjusted low and high cut-off frequencies. Three kinds of hot-wire probes were used. The first, for mean velocity measurements, was a straight wire mounted on jeweller's broaches, encased in Nu-Weld dental cement, with 6 mm stainless-steel tube as the main shaft. The sensitive part was 4 μm in diameter, 1·5 mm long and made of platinum–rhodium (10 % rhodium) etched from Wollaston type after the silver coating had been soldered to the tips of the broaches. The second type, for measurements of the decay of the three components of turbulence intensity, was a special Disa type 55A38, 2·5 μm, Pt-plated tungsten X-wire. The length of the sensitive part was 1·25 mm and the distance between the two wires was less than 1 mm. The third type, used for $\overline{u^2}$-spectrum measurements, was a Disa type 55F01, 5 μm, Pt-plated tungsten, straight wire. The length of the sensitive part was 1·25 mm.

The spectral distribution of the energy associated with the streamwise fluctuations was measured with two kinds of filters, depending upon the frequency range of interest. For the range 1–200 Hz, a Dytronics model 720 band-pass filter was used. The unit employs a Wien bridge degenerative feedback

† Ratio of rod outside diameter to mesh size.

‡ American Standard no. 110 MH, series 106 industrial centrifugal fan.

§ American Standard class 2, no. 76-615-F3.

network, and has a bandwidth proportional to the nominal frequency. It was used in the low selectivity mode (bandwidth = ± 18 % of the centre frequency, to the '3 db down' points). In the higher frequency range, 100 Hz–10 kHz, this band was too large for our purposes, so a Hewlett-Packard model 302A (constant bandwidth) wave analyser was used. It has a bandwidth of ± 3·5 c/s at least 3 db down, and ± 25 c/s at least 50 db down. Calibration curves are reported by Comte-Bellot & Corrsin (1971). The outputs of the two units were matched at 100 c/s.

3. Flow near the grid

For a passive grid at moderate rod Reynolds numbers, with solidity below the unstable range, the wakes of the individual bars become turbulent close behind the grid, spread individually, and interact in some complicated way, eventually merging so that, at a large number of mesh lengths from the grid (e.g. $x/M > 30$), the turbulence is nearly homogeneous laterally. It is also nearly isotropic. In the jet grid the situation is made even more complicated by the additional interactions with the jets issuing from the rods.

For simplicity, we start the descriptions with a passive grid consisting of parallel rods of any (single) shape. If the wakes of the individual bars (or the jets of the individual slots) gradually merge without lateral axis shifts, we can expect that an accurately made grid will generate a field with reasonably good transverse homogeneity far downstream. This is not the case, however, when the grid solidity, i.e. the fraction of duct area blocked, is sufficiently great. The wake system then is *unstable* in the large. The individual wakes (or jets) coalesce successively into larger and larger wakes (or jets). The resulting turbulence is not only of larger scale and more intense than in the stable case, but is less likely to be transversely homogeneous. Even the mean velocity profile may never become uniform before the wall boundary layers take over the duct (Von Bohl 1940; Corrsin 1944, 1963). The effective fluid-dynamic solidity of the grid presumably determines the downstream stability of the flow system. The separation-point location on each rod influences the value of this solidity, so grids of square or rectangular rods are less sensitive to changes in the Reynolds number. For round rods, the separation location depends on the Reynolds number. For rod Reynolds numbers from 10^3 to 10^5, the boundary-layer separation is laminar, although the wake is turbulent. The location of this laminar separation is at 80–85° from the upstream stagnation point (e.g. Chang 1966, p. 5). Accordingly, over that range of rod Reynolds numbers, even a round-rod (passive) grid would have an approximately constant static pressure drop coefficient, hence an approximately constant turbulence level at any prescribed distance downstream.

For jet grids, we can distinguish two cases: the first when the jets are directed downstream (coflow injection), the second when they are directed upstream (counterflow injection). Downstream jets have been used in boundary-layer control (e.g. Hoerner 1965, pp. 3–26). They can be used to reattach an otherwise separated boundary layer, or to delay the separation. They do that by reducing the severity of the adverse pressure gradient in the boundary layer. By a similar

mechanism, the jets on each grid rod, through entrainment effects, reduce the rod wake width, hence lower the effective solidity, and reduce the static pressure drop across the grid.† This can lead to a smaller turbulence level at a prescribed distance downstream, unless the jet strength is so large that the level increases again.

To see the entrainment effect (and the counterflow case as well), a hydrogen-bubble flow visualization technique was used on rod models in a 30×23 cm water tunnel (Karweit & Corrsin 1969). A single jet rod was set with its axis perpendicular to the flow direction. Secondary water was ejected from the jet. Figure 2 (plate 2) shows two hydrogen-bubble pictures. In the first one, with no injection, the boundary layer is separated locally‡ at the wing-nut used to control the jet needle valve. In the second one, with a coflowing jet (left to right) at the wind-tunnel equivalent of a 5 % injection ratio, the wake is clearly narrower and the effective solidity is smaller.

As we increase the jet speed, the turbulent energy developed from the large mean flow kinetic energy of the jets can more than counteract the previously explained turbulence-reducing effects of the jets. For still higher jet strength, the system becomes unstable, jets coalesce, and large regions of reverse flow can be found. Then the effective solidity is larger and the turbulence scales become larger, with an inevitable rise in the turbulence levels.

In the second case, the jets are directed upstream (counterflow injection). Jets blowing upstream penetrate a distance (linearly) proportional to the relative jet strength (Rouse 1956). Then the main flow must go around the 'stagnant' eddies formed by the penetrating jets. Consequently, the effective or 'apparent' solidity increases monotonically with increasing jet strength. That yields a larger static pressure drop across the grid§ and larger turbulence levels. For high enough jet strengths, the flow system becomes unstable (like that behind the high solidity passive grid), with turbulence not only of larger scale and more intense than in the stable case, but also less likely to be transversely homogeneous.

Figure 3 (plate 3) shows two hydrogen-bubble pictures, the first one with no injection, the second one with 5 % equivalent counterflow injection. The general flow is from left to right. The effective solidity is clearly increased (second picture) by counterflow injection.

4. Static pressure drop across the grid

In order to estimate the mean drop in static pressure across a grid, consider one element (one mesh) of the grid, as shown in figure 4. We assume that the jets are directed downstream, that the static pressure P and the mean velocity U are uniform far away from the grid, that the boundary layers are thin, and

† The static pressure drop across the grid decreases owing to a combination of the above mentioned effect and the total (coflowing) jet thrust, though the two effects are coupled.

‡ For the rest of the rod, the separation point is at 80–85° from the upstream stagnation point.

§ Again, this is due to a combination of the wake widening effect and the 'negative' jet thrust.

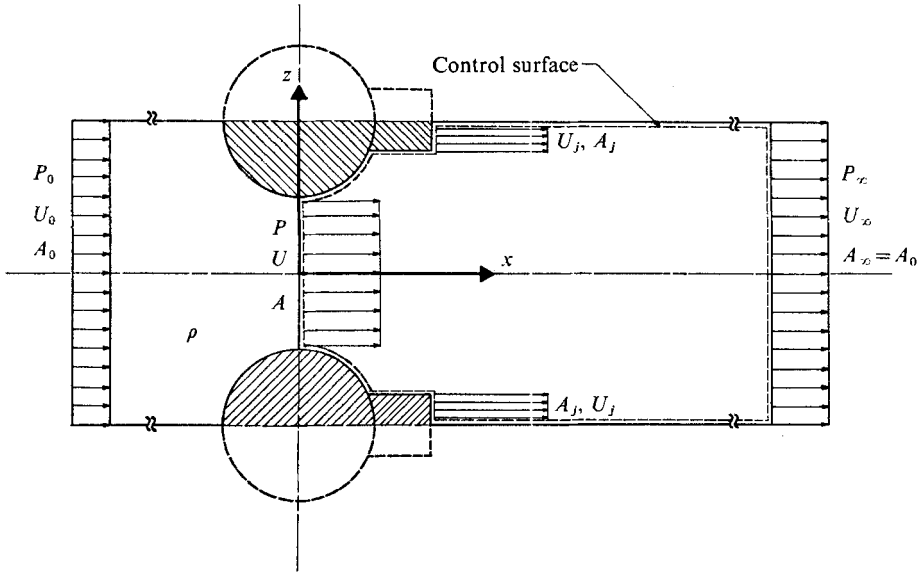

FIGURE 4. Model for the flow through the grid.

that they separate at the 'throat'. We neglect viscous forces and body forces. The (constant) density is ρ and A is the throat area. Using Bernoulli's equation and the continuity equation up to the throat, we get

$$\frac{P_0-P}{\rho} = \frac{U_0^2}{2}\left[\left(\frac{A_0}{A}\right)^2 - 1\right]. \tag{1}$$

Applying the gross momentum balance† from the throat to a station far downstream, and assuming 'sudden expansion' flow, we get

$$\frac{P-P_\infty}{\rho} \approx U_\infty^2 - U^2\frac{A}{A_\infty} - U_j^2\frac{A_j}{A_\infty}. \tag{2}$$

We add (1) and (2) and introduce the following definitions:

$$\text{geometrical solidity} = \sigma \equiv (A_0-A)/A_0, \tag{3}$$

$$\text{coefficient of static pressure drop} = C_p \equiv (P_0-P_\infty)/\tfrac{1}{2}\rho U_0^2, \tag{4}$$

$$\text{injection ratio} = J \equiv Q_j/Q_0 = U_jA_j/U_0A_0, \tag{5}$$

$$\text{area ratio} = R \equiv A_0/A_j. \tag{6}$$

Then, after some algebra, we get

$$C_p \approx \left(\frac{\sigma}{1-\sigma}\right)^2 + 2J^2\left(1+\frac{2}{J}-R\right). \tag{7}$$

When there is no injection ($J = 0$), this reduces to $C_p \approx [\sigma/(1-\sigma)]^2$, as derived before by Harris (1965), for a passive grid.

To test (7), we measured the static pressure at the walls of the wind tunnel, $2{\cdot}5M$ upstream and $7M$ downstream of the grid, at various injection ratios.

† See, for example, Prandtl & Tietjens (1934, p. 233).

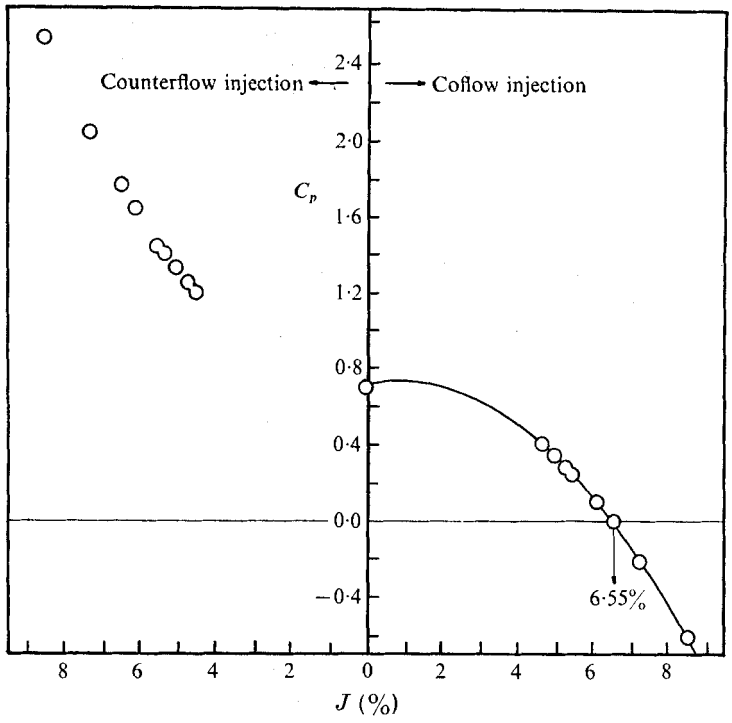

FIGURE 5. Effect of injection on C_p. ○, experiment; ——, equation (7).

The estimated error of these measurements is about ± 2 %.† In figure 5, equation (7) is plotted (for coflow injection only), along with the experimental results (for both coflow and counterflow injection). The experiment agrees with (7), within 5 %, when the first term on the right-hand side is multiplied by 2·01, an empirical normalization constant which depends on the grid geometry and presumably compensates for the difference between the geometric and aerodynamic solidities.

For the passive grid ($J = 0$), C_p is approximately constant over the range of rod Reynolds numbers $R_D \equiv U_0 D/\nu$ covered by the experiment ($10^3 < R_D < 10^5$). The same result has been observed by Naudascher & Farell (1970).

Coflow injection reduces the static pressure drop across the grid, and counterflow injection increases it. We notice that the static pressure drop is zero when the (coflow) injection ratio is 6·55 %. For stronger coflow injection, C_p changes sign and the static pressure rises across the grid.

The net force F exerted by the grid on the air might be thought of as a combination of drag and thrust forces, although a clear separation is not possible. If the net force on the air is in the main flow direction ($F > 0$), then the grid has a net 'thrust'. If it is opposite to the main flow direction ($F < 0$), then the grid has a net 'drag'.

† The day-to-day repeatability was within ± 1%; the rest of this error estimate is really a guess based on prior experience with similar experiments and on order-of-magnitude estimates of the behaviour of orifices and manometers in the presence of disturbances.

It can be shown (Gad-el-Hak 1972) by applying the gross momentum balance on a control volume bounded by stations far upstream and downstream of the grid, and considering the grid as a 'momentum source', that

$$C_F \doteq 2J(2+J) - C_p, \tag{8}$$

where

$$C_F \equiv F/\tfrac{1}{2}\rho U_0^2 A_0. \tag{9}$$

Equation (8) provides a method for determining the force on the grid, provided that we know C_p. For the passive grid ($J = 0$), we get equal coefficients of pressure and force ($C_F = -C_p$); the force is purely a drag force. Weak coflow injection yields a negative force, i.e. the grid has net drag. Strong coflow injection yields a positive force, i.e. the grid has net thrust, and a particular injection ratio ($J = 5{\cdot}56$ %)† yields zero force; then the grid is *self-propelled*. We note that zero static pressure drop does not imply zero force. Counterflow injection makes C_F become monotonically more negative (net drag).

5. Homogeneity and isotropy of the flow field in the test section

The degree of homogeneity and isotropy attained in the flow field downstream of the jet grid is important if we are to interpret the experimental results in the light of isotropic turbulence theory. One requirement is uniformity of mean velocity profiles in the test section. Lacking exact uniformity, we must estimate the relative magnitudes of the energy 'production' terms in the general turbulence kinetic energy equation. Further requirements are uniformity of the profiles of more complicated statistical quantities, such as the root-mean-square velocity fluctuations (u', v' and w'). Streamwise inhomogeneity of the turbulence is, of course, unavoidable, but its dimensionless measure decreases as we go farther from the grid (see, for example, Corrsin 1963).

Mean velocity profiles were measured at several downstream sections, from about 30 mesh lengths from the grid, where the individual wakes and jets were no longer detectable, to about 90 mesh lengths from the grid. For the zero-injection and the coflow-injection cases, the profiles were flat with less than 2 % *deviation* in the core region (about half the cross-sectional area of the test section). For the counterflow-injection cases, the deviation was as high as 5 %, which indicates possible instability of the jet system. However, all profiles are significantly improved over past jet-grid experiments [15 % in the Mathieu & Alcaraz experiment (1965), 15 % in the Teunissen experiment (1969), 30 % in the Luxenberg & Wiskind experiment (1969) and 10 % in the Liu *et al.* experiment (1971)]. The high degree of inhomogeneity in those experiments may have resulted not only from 'obvious' causes such as residual free-stream effects or grid inaccuracies and jet 'manifold' non-uniformities, but also from instabilities of the jet systems after they emerged.

A typical production term in the turbulence kinetic energy equation (e.g. $-\overline{uv}/\partial\overline{U}/\partial y$) was less than one-hundredth of the rate of dissipation ϵ of kinetic energy per unit mass. Production is clearly negligible.

† The estimated error in determining the injection ratio necessary to yield a self-propelled grid is ± 2%.

u', v' and w' profiles were less flat than the mean velocity profiles, with a maximum deviation of about 8 %. Indeed, the more complex a statistical quantity is, the more sensitive it might be to grid inaccuracies, residual free-stream turbulence non-uniformity and a non-uniform distribution of jet strength.

Another requirement for isotropy is the equality of r.m.s. turbulence components in all directions. Typically u' and w' were of the same order (within 5 %) and about 15 % larger than v', something that we expect from a grid of parallel rods.† No clear trend towards more or less isotropy with distance from the grid is observed.

Details of the effects of injection on the degree of homogeneity and isotropy attained in the flow field downstream of the jet grid are available (Gad-el-Hak 1972).

6. Turbulence levels

In §4, we related the static pressure drop across the grid to the grid geometrical solidity. For example, for a passive grid ($J = 0$),

$$C_p \approx [\sigma/(1-\sigma)]^2. \tag{10}$$

The fluid passing through the (passive) grid accelerates from U_0, say, to about $U_0/(1-\sigma)$.

If we assume naively that the r.m.s. turbulence velocity component u' at any prescribed distance from the grid is related to the difference between the mean velocity through the grid and the mean velocity upstream, use (10) and rearrange, we get

$$U_0^2/\overline{u^2} \sim 1/C_p. \tag{11}‡$$

A slightly more sophisticated *ad hoc* assumption is that the average kinetic energy flux emerging from the (passive) grid is proportional to the sum of the fluxes of mean flow kinetic energy and turbulence kinetic energy at any prescribed distance from the grid. This assumption gives

$$\frac{U_0^2}{\overline{u^2}} \sim \frac{1}{C_p + 2\sqrt{C_p}}. \tag{12}$$

The 'constant' of proportionality would include the x dependence.

For a jet grid no such simple relation can be derived. Other factors like the effects of injection on the boundary layers around the grid elements, the turbulence levels near the jet exits, and the stability of the system of jets must be considered.

For the jet grid the secondary air flow was fixed at 1460 ft^3/min (0·69 m^3/s), ± 1 %, and the primary air flow was varied as a means of varying the injection ratio J.§ Varying the flow of secondary air would have required readjustment of all throttles. The injection ratio was varied between 4·7 % and 8·55 %,

† Vortex sheets and lines shed by the rods tend to be parallel to them.

‡ This was assumed, without proof, by Batchelor (1953, p. 135) and Harris (1965).

§ Ratio of total jet ('secondary') volumetric flow rate to primary air flow rate.

U_0 (m/s)	U_∞ (m/s)	$\overline{U}$ (m/s)	J (%)	R_M ($\times 10^{-4}$)
5·69	6·18	7·81	8·55	4·18
6·65	7·14	9·02	7·32	4·83
7·43	7·92	10·01	6·55	5·36
7·95	8·44	10·67	6·12	5·72
8·76	9·25	11·69	5·56	6·26
9·11	9·60	12·13	5·34	6·50
10·36	10·84	13·70	4·70	7·34

TABLE 1. Mean velocities and injection ratios

corresponding to variation in the mean velocity in the test section between 13·7 m/s and 7·81 m/s, respectively.

Table 1 lists the injection ratios J and the corresponding mean velocities upstream (U_0) and downstream (U_∞) of the grid, and in the test section ($\overline{U}$).† It also shows the corresponding mesh Reynolds number $U_\infty M/\nu$. For the passive grid, $J = 0$, $U_0 = U_\infty$ and the Reynolds numbers are the same as those listed in the table.

The $\overline{u^2}$, $\overline{v^2}$ and $\overline{w^2}$ data give $\overline{q^2}$ [$\equiv \overline{u^2}+\overline{v^2}+\overline{w^2}$] and $q'/\overline{U}$, where the prime denotes a root-mean-square value. Figure 6 shows the effects of injection on $\overline{q^2}$ at $x/M = 30$ and 81. When there is no injection, $\overline{q^2}$ may still vary with Reynolds number. To see more clearly the effects of injection on turbulence energy, we plot on the same figure $\overline{q^2}$ for the zero-injection case with the horizontal axis representing R_M^{-1} instead of J. $J \sim R_M^{-1}$ because the jet flow rate was held constant throughout the $J \neq 0$ cases.

Weak coflow injection reduces the turbulence energy at any fixed x/M.‡ For strong coflow injection, the additional turbulence and shear in the jets themselves become more than enough to counteract the effect of the width decrease in rod wakes. At higher injection ratios still, the jet system becomes unstable and much higher turbulence intensities are observed. With counterflow injection, the turbulence energy is high, and the effect is still more pronounced at high injection ratios. Counterflow injection evidently increases the effective solidity of the grid, experiences instability at relatively small J, and/or changes the 'effective position' of the grid.

The effects of injection on the turbulence levels at $x/M = 30$ and 81 are shown in figure 7. The behaviour of $q'/\overline{U}$ (%) can best be visualized by comparing (in figure 6) $\overline{q^2}$ for the active and the passive modes at the same R_M^{-1} (or mean velocity in the test section). For weak coflow injection, the turbulence level is lower than in the zero-injection case. For strong coflow injection, the turbulence level is higher than in the zero-injection case. For the counterflow injection, the turbulence level is always higher than in the zero-injection case, an effect which is more pronounced for strong injection. For the passive grid, $q'/\overline{U}$ is approximately constant in the range of Reynolds numbers used in the experiment. Therefore, no vertical bars were required in this figure.

† A slight contraction was used to improve the isotropy of the flow.

‡ See §3.

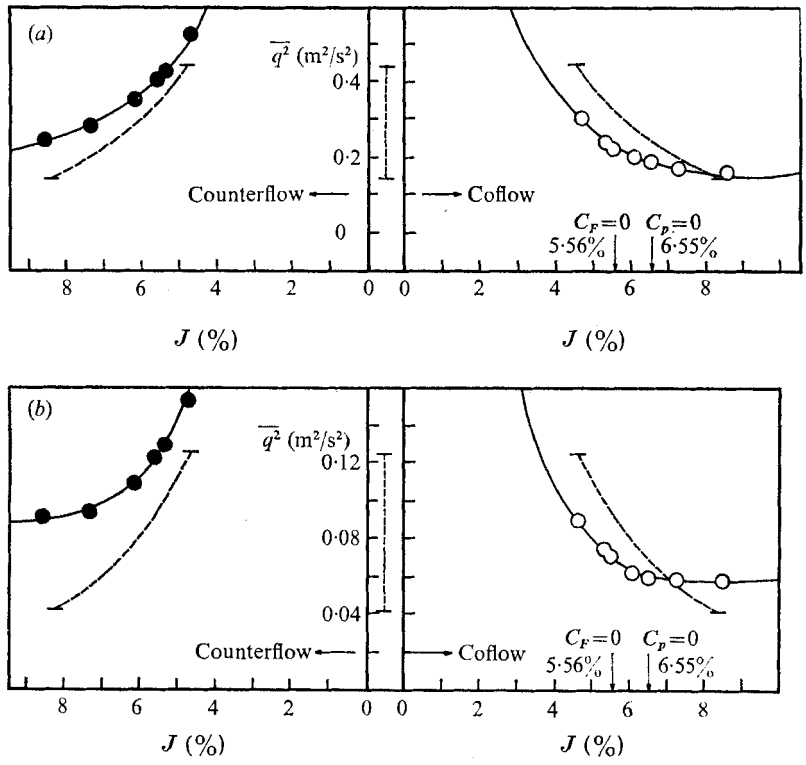

FIGURE 6. Effects of injection on $\overline{q^2}$. (*a*) $x/M = 30$. (*b*) $x/M = 81$. ⊖, coflow injection; -●-, counterflow injection; – – – –, zero injection.

7. Decay of turbulence

Using the X-configuration hot wire, we measured the $\overline{u^2}$, $\overline{v^2}$ and $\overline{w^2}$ decay histories from the end of the secondary contraction (about $20M$ from the grid) to about $90M$ from the grid. A good approximation to homogeneity occurred at about $30M$ from the grid and beyond. We consider only the data in that region.

Corrections for finite hot-wire length were negligible.† Corrections for background (no grid) velocity fluctuations, for possible air temperature fluctuations and for electronic noise were all made by subtracting from the mean-square total signal the mean-square signal in the empty tunnel at the same position, speed and hot-wire condition.

In each run, 30 readings were taken traversing the hot wire monotonically away from the grid, then 30 more readings traversing back upstream. The repeatability of the u', v' and w' values in a single run was within ± 2 %. However, the repeatability from day to day was only within 4 %. A technique for minimizing this effect was mentioned by Comte-Bellot & Corrsin (1966).

Figure 8 is a typical logarithmic decay plot of $\overline{U}^2/\overline{u^2}$, $\overline{U}^2/\overline{v^2}$ and $\overline{U}^2/\overline{w^2}$ versus x/M, for a coflow-injection ratio of 4·7 %, for a counterflow-injection ratio 8·55 %

† The sensitive wire length is about three times the Kolmogoroff length scale. See, for example, Wyngaard (1968, 1969).

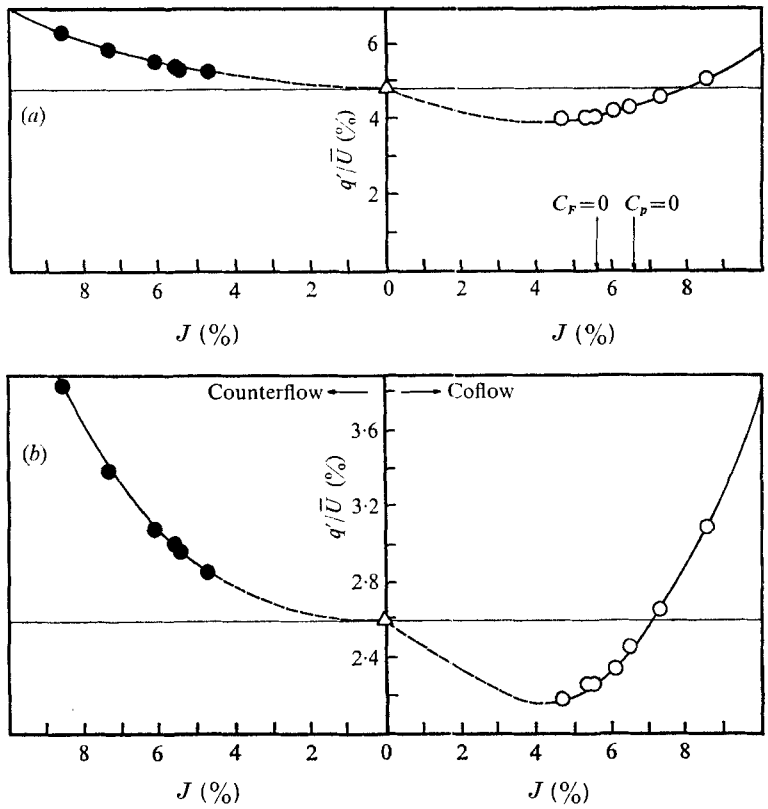

FIGURE 7. Effects of injection on $q'/\bar{U}$. (*a*) $x/M = 30$. (*b*) $x/M = 81$. ⊖, coflow injection; ●, counterflow injection; △, zero injection.

and for zero injection ($R_M = 7{\cdot}34 \times 10^4$). Of this group, the counterflow yields the highest turbulence levels, while the coflow yields the lowest.

The fact that these plots are approximately linear suggests that the decay obeys the 'empirical' power law

$$\bar{U}^2/\overline{u^2} = B(x/M)^n, \tag{13}$$

or, inspired by (11),

$$\frac{\bar{U}^2}{\overline{u^2}} = \frac{b}{C_p}\left(\frac{x}{M}\right)^n, \tag{14}$$

where $\bar{U} \equiv$ mean velocity in the test section, $\overline{u^2} \equiv$ mean-square velocity fluctuation in the longitudinal direction, B and b are constants and n is the decay exponent. Similar equations can be written for $\overline{v^2}$ and $\overline{w^2}$ decay.

Before arriving at this specific form, we first plotted

$$\bar{U}^2/\overline{u^2} \text{ (or } \bar{U}^2/\overline{v^2} \text{ or } \bar{U}^2/\overline{w^2}) \text{ versus } x/M - x_0/M$$

on log paper, using different values of x_0 (location of 'apparent' origin), and used the value which yields the longest straight line.† $x_0 = 0$ was quite satisfactory

† The viewpoint here is simply to seek the 'best' power law to fit the data. We do not mean to imply that the turbulent energy must decay as a power law on any persuasive theoretical grounds.

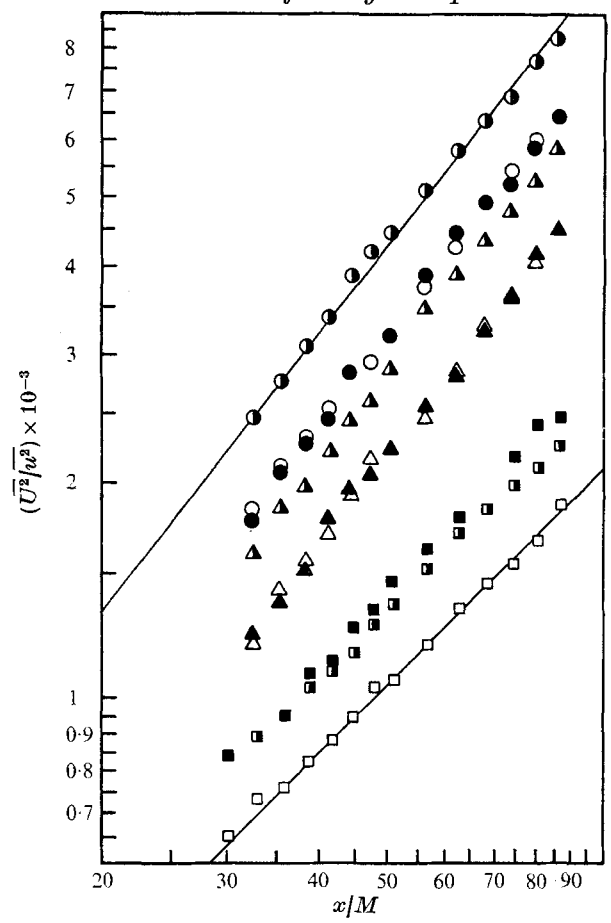

FIGURE 8. $\overline{u^2}$, $\overline{v^2}$ and $\overline{w^2}$ decay. Coflow injection, 4·7%: ○, $\overline{u^2}$ decay; ◑, $\overline{v^2}$ decay; ●, $\overline{w^2}$ decay. Counterflow injection, 8·55%: □, $\overline{u^2}$ decay; ◨, $\overline{v^2}$ decay; ■, $\overline{w^2}$ decay. Zero injection: △, $\overline{u^2}$ decay; ◭, $\overline{v^2}$ decay; ▲, $\overline{w^2}$ decay.

and yielded a straight line in almost all cases tested. These x_0/M values have an estimated accuracy of $\pm 1{\cdot}0$. No point deviated from that straight line (on the log plot) by more than $\pm 0{\cdot}7$ %.

Preliminary measurements showed a dependence of n on the injection ratio. The changes in n were small, necessitating extreme care in determination. Among the error sources are the choice of the apparent origin x_0, the short x-range of measurements, the small number of data points and the difficulty of measuring the slopes.

Using a Leasco time-sharing digital computer, we devised a least-squares subroutine to determine B and n. The estimated accuracy in B is ± 4 %, and in n is $\pm 0{\cdot}01$.

Figure 9 shows the dependence of the exponents of $\overline{u^2}$, $\overline{v^2}$ or $\overline{w^2}$ decay on the injection ratio J. For coflow injection at each J, n is nearly the same for all three components. For the counterflow injection this is not the case, consistent with the lower degree of isotropy.

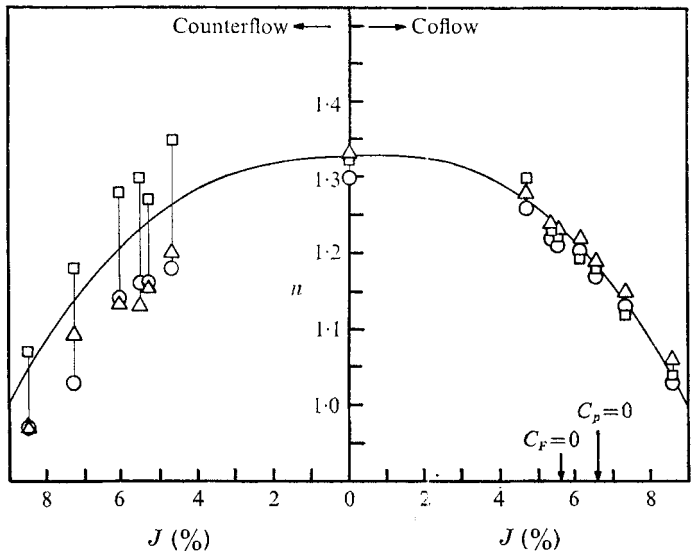

FIGURE 9. Exponent of decay and injection ratio.
○, $\overline{u^2}$ decay; △, $\overline{v^2}$ decay; □, $\overline{w^2}$ decay.

The principal result here perhaps is the monotonic decrease of n with increasing injection ratio, for both coflow and counterflow. Stronger injection yields slower decay. Does the turbulence generated by injection have relatively more energy in the low wavenumber region (large eddies) and, accordingly, decay more slowly?† The spectral data presented in the next section suggest that the answer is no, at least in the range $x/M \geqslant 30$. As a matter of fact, injection seems to improve energy transfer to the high wavenumber region. Perhaps the explanation lies in details of the dynamical interactions near the grid. A detailed investigation in this inhomogeneous anisotropic region might shed some light on the behaviour of the decaying homogeneous turbulence further from the grid.

We notice that the (coflow) injection ratios corresponding to zero force ($J = 5{\cdot}56\,\%$) and zero static pressure drop ($J = 6{\cdot}55\,\%$) do not yield, within our experimental resolution, any singular behaviour. $n(J)$ is smooth and monotonic whether the grid experiences a net average drag force, or net average thrust force or zero average force. This is different from the decay of the wake behind a single body in an 'infinite' flow. If the body is self-propelled, its wake decays at a rate different (higher) from that for a body with net drag or net thrust (see Naudascher 1965; Tennekes & Lumley 1972, p. 124). Furthermore, the wake asymptotic decay rate for a single body has the same exponent for any net value of the thrust or drag coefficient. Of course, exact correspondence between the two cases is not expected; after all, the field behind a single body is inhomogeneous, while the field (far) behind the grid is homogeneous. The former has continuous production of energy while the latter does not.

† Tsuji (1955) proposed a smaller n for turbulence which contains superposed low frequency components.

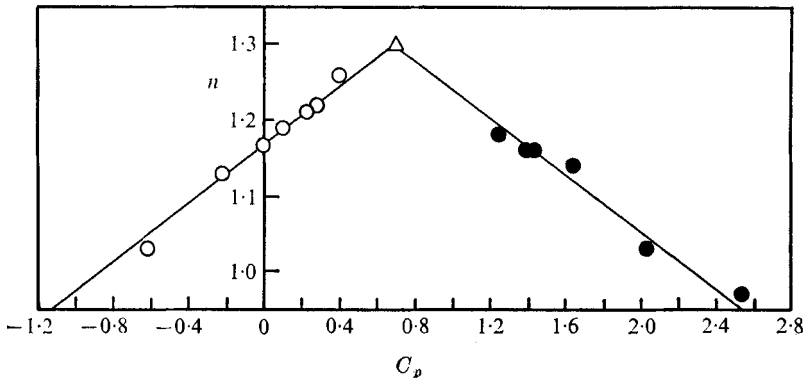

FIGURE 10. Exponent of decay and C_p. ○, coflow injection; ●, counterflow injection; △, zero injection.

For coflow injection ratios higher than 8·55 %, the flow showed 'symptoms' of instability (inhomogeneity, etc.). The turbulence levels increased considerably, and the exponent of decay increased and became as high as 1·70.† The 'symptoms' were clear at the highest injection ratio 18·9 %.‡ These data are not reported here, since this report is concerned with nearly isotropic, hence nearly homogeneous, turbulence.

For counterflow injection the symptoms of instability appeared even for $J < 8{\cdot}55$ %, so the results for this mode should be reviewed cautiously.

Table 2 lists the values of n, B and b ($\overline{u^2}$, $\overline{v^2}$ and $\overline{w^2}$ decay) for various cases. They are approximately constant over this range of R_M (for the passive grid). There are small differences among the decays of $\overline{u^2}$, $\overline{v^2}$ and $\overline{w^2}$ (in perfectly isotropic turbulence, n, B and b must of course be the same for all three components). The table also includes the results reported by Corrsin (1942), Batchelor & Townsend (1947, 1948*a*), Baines & Peterson (1951), Tsuji & Hama (1953), Wyatt (1955), Kistler & Vrebalovich (1961), Uberoi (1963), Harris (1965), Comte-Bellot & Corrsin (1966), Guillon (1968),§ Luxenberg & Wiskind (1969)§ and Liu *et al.* (1971).§

The effect of the static pressure drop across the grid on the exponent of $\overline{u^2}$ decay is examined in figure 10. No monotonic behaviour is observed, and the $C_p = 0$ case does not stand out. Notice the nearly symmetric behaviour of the coflow and the counterflow cases.

† Of course, this cannot be interpreted to mean that the turbulent energy decays more rapidly in this inhomogeneous field than in the (stable) homogeneous cases. Averaging in some sense over the cross-section, we can write a kinetic energy balance equation in a moving frame as $d(\frac{1}{2}\overline{q^2})/dt \approx P - \epsilon$, where P and ϵ are mean production and dissipation rates. For given turbulent fine-structure (at any t), ϵ is given, and the most rapid decay must occur when $P = 0$ (the transversely uniform case).

‡ The wind-tunnel fan was stopped completely, and the flow rate in the test section was the sum of the jet flow rate and the entrained air flow rate.

§ Jet grid.

Source, type of grid and solidity	R_M ($\times 10^{-4}$)	J (%)	$\overline{u^2}$ decay			$\overline{v^2}$ decay			$\overline{w^2}$ decay		
			n	B	b	n	B	b	n	B	b
Present work	4·18	8·55	1·03	27·3	−16·9	1·06	31·7	−19·7	1·04	35·4	−21·9
	4·83	7·32	1·13	28·7	−6·3	1·15	34·0	−7·5	1·12	29·9	−6·6
Jet grid (coflow injection)	5·36	6·55	1·17	30·2	0·0	1·19	32·0	0·0	1·18	27·0	0·0
	5·72	6·12	1·19	29·6	3·0	1·22	31·0	3·1	1·20	25·6	2·6
	6·26	5·56	1·21	26·9	6·2	1·22	32·0	7·4	1·23	25·4	5·8
$\sigma = 0{\cdot}37$	6·50	5·34	1·22	27·3	7·6	1·24	30·7	8·6	1·23	25·8	7·2
	7·34	4·70	1·26	23·1	9·2	1·28	27·9	11·2	1·30	20·9	8·4
Present work	4·18	8·55	0·97	24·1	61·0	0·97	30·3	76·7	1·07	21·4	54·1
	4·83	7·32	1·03	23·8	48·3	1·09	23·7	48·1	1·18	17·0	34·5
Jet grid (counterflow injection)	5·72	6·12	1·14	18·9	31·0	1·14	22·1	36·2	1·28	12·4	20·3
	6·26	5·56	1·16	18·6	26·6	1·13	24·3	34·7	1·30	12·2	17·4
	6·50	5·34	1·16	19·6	27·2	1·16	21·9	30·4	1·27	13·5	18·8
$\sigma = 0{\cdot}37$	7·34	4·70	1·18	19·0	23·6	1·20	19·4	24·1	1·35	10·1	12·5
Present work	4·83	0	1·32	13·2	9·1	1·33	15·9	11·0	1·29	14·5	10·0
Jet grid (zero injection)	5·72	0	1·32	14·1	10·2	1·31	16·5	11·9	1·34	13·3	9·6
	6·26	0	1·30	14·8	10·2	1·32	16·3	11·2	1·35	12·0	8·3
$\sigma = 0{\cdot}37$	6·50	0	1·28	15·0	10·9	1·35	14·2	9·9	1·32	12·4	8·7
	7·34	0	1·30	13·8	9·7	1·33	15·3	10·7	1·34	11·3	7·9
Corrsin (1942)											
Biplane, round rods											
$\sigma = 0{\cdot}44$	0·85	0	1·30	20·0	—	1·22	59·0	—	—	—	—
$\sigma = 0{\cdot}44$	1·70	0	1·28	23·0	—	1·14	62·0	—	—	—	—
$\sigma = 0{\cdot}44$	2·60	0	1·35	17·0	—	1·16	58·0	—	—	—	—

TABLE 2. Turbulence energy decay

Source, type of grid and solidity	R_M ($\times 10^{-4}$)	J (%)	$\overline{u^2}$ decay			$\overline{v^2}$ decay			$\overline{w^2}$ decay		
			n	B	b	n	B	b	n	B	b
Batchelor & Townsend (1947, 1948*a*)											
Biplane, round rods											
$\sigma = 0{\cdot}34$	0·55	0	1·13	70·0	—	—	—	—	—	—	—
$\sigma = 0{\cdot}34$	1·10	0	1·25	48·0	—	—	—	—	—	—	—
Baines & Peterson (1951)											
Biplane, square rods											
$\sigma = 0{\cdot}44$	2·40	0	1·37	8·5	—	—	—	—	—	—	—
Tsuji & Hama (1953)											
Biplane, round rods											
$\sigma = 0{\cdot}36$	3·30	0	1·35	10·0	—	—	—	—	—	—	—
Wyatt (1955)											
Biplane, round rods											
$\sigma = 0{\cdot}34$	1·10	0	1·27	31·0	—	—	—	—	—	—	—
$\sigma = 0{\cdot}34$	2·20	0	1·27	35·0	—	—	—	—	—	—	—
$\sigma = 0{\cdot}34$	4·40	0	1·25	35·0	—	—	—	—	—	—	—
Kistler & Vrebalovich (1961)											
Biplane, round rods											
$\sigma = 0{\cdot}34$	242·00	0	1·00	71·0	—	1·00	110·0	—	—	—	—

TABLE 2 (*cont.*)

Source, type of grid and solidity	R_M ($\times 10^{-4}$)	J (%)	$\overline{u^2}$ decay n	B	b	$\overline{v^2}$ decay n	B	b	$\overline{w^2}$ decay n	B	b
Uberoi (1963)											
Biplane, round rods											
$\sigma = 0{\cdot}44$	2·90	0	1·20	24·0	—	1·20	35·0	—	—	—	—
Harris (1965)											
Parallel, round rods											
$\sigma = 0{\cdot}13$	1·18	0	1·67	—	—	1·62	—	—	1·51	—	—
$\sigma = 0{\cdot}19$	1·15	0	1·52	—	—	1·60	—	—	1·74	—	—
$\sigma = 0{\cdot}25$	0·82	0	1·43	—	—	1·45	—	—	1·45	—	—
$\sigma = 0{\cdot}29$	2·64	0	1·14	—	—	1·45	—	—	1·25	—	—
$\sigma = 0{\cdot}31$	0·61	0	1·34	—	—	1·23	—	—	1·44	—	—
$\sigma = 0{\cdot}38$	1·82	0	1·43	—	—	1·33	—	—	1·39	—	—
Comte-Bellot & Corrsin (1966)											
Biplane, square rods											
$\sigma = 0{\cdot}34$	1·70	0	1·29	19·0	—	1·28	18·0	—	—	—	—
$\sigma = 0{\cdot}34$	3·40	0	1·27	20·0	—	1·29	19·0	—	—	—	—
$\sigma = 0{\cdot}34$	6·80	0	1·25	22·0	—	1·27	19·0	—	—	—	—
$\sigma = 0{\cdot}34$	13·50	0	1·15	29·0	—	1·16	28·0	—	—	—	—
Biplane, round rods											
$\sigma = 0{\cdot}44$	3·40	0	1·24	35·0	—	1·24	34·0	—	—	—	—
$\sigma = 0{\cdot}44$	6·80	0	1·26	34·0	—	1·27	32·0	—	—	—	—
Disks											
$\sigma = 0{\cdot}31$	3·40	0	1·32	7·1	—	1·52	7·5	—	—	—	—
$\sigma = 0{\cdot}31$	6·80	0	1·33	7·9	—	1·30	9·7	—	—	—	—

TABLE 2 (*cont.*)

Source, type of grid and solidity	R_M ($\times 10^{-4}$)	J (%)	$\overline{u^2}$ decay			$\overline{v^2}$ decay			$\overline{w^2}$ decay		
			n	B	b	n	B	b	n	B	b
Guillon (1968)											
Jet grid											
$\sigma = 0{\cdot}51$	11·42	4·40	1·27	—	—	—	—	—	—	—	—
Luxenberg & Wiskind (1969)											
Jet grid											
$\sigma = 0{\cdot}44$	0·65	0	1·31	—	—	—	—	—	—	—	—
$\sigma = 0{\cdot}44$	0·69	2·35	1·03	—	—	—	—	—	—	—	—
$\sigma = 0{\cdot}44$	0·65	2·98	1·08	—	—	—	—	—	—	—	—
$\sigma = 0{\cdot}44$	0·65	3·87	1·35	—	—	—	—	—	—	—	—
$\sigma = 0{\cdot}44$	0·65	4·33	1·69	—	—	—	—	—	—	—	—
Liu *et al.* (1971)											
Jet grid											
$\sigma = 0{\cdot}44$	0·65	0	1·45	—	—	—	—	—	—	—	—
$\sigma = 0{\cdot}44$	0·65	1·92	1·02	—	—	—	—	—	—	—	—
$\sigma = 0{\cdot}44$	0·65	2·99	0·86	—	—	—	—	—	—	—	—
$\sigma = 0{\cdot}44$	0·65	3·56	2·02	—	—	—	—	—	—	—	—
$\sigma = 0{\cdot}44$	0·65	5·25	2·48	—	—	—	—	—	—	—	—
$\sigma = 0{\cdot}44$	0·65	5·64	3·37	—	—	—	—	—	—	—	—

TABLE 2 (*cont.*)

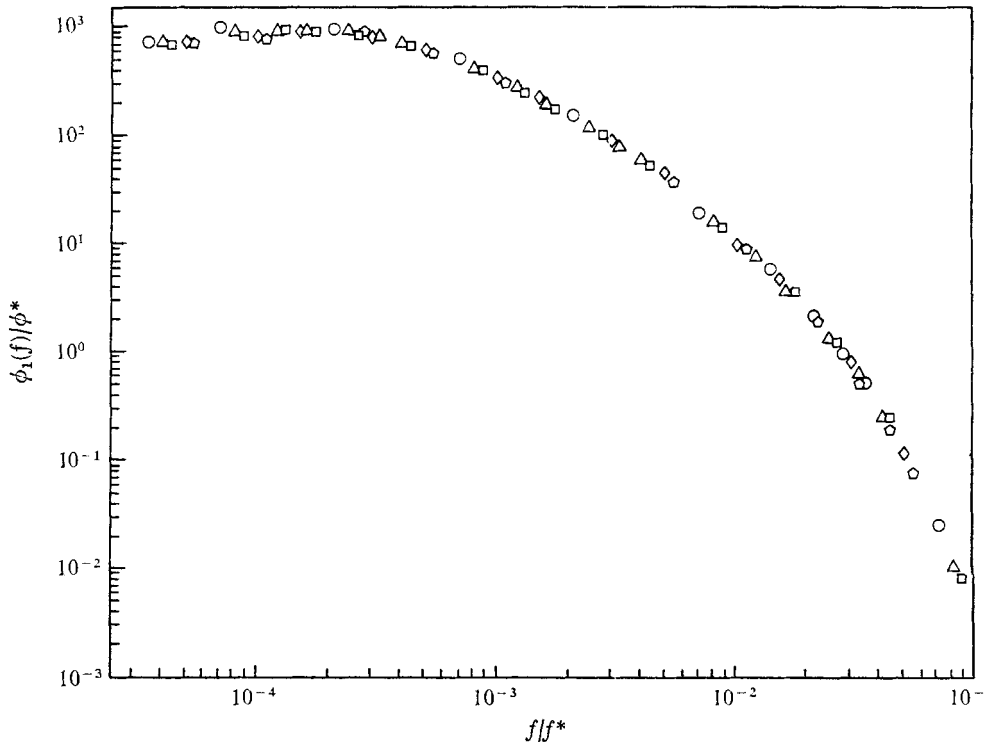

FIGURE 11. Normalized one-dimensional energy spectra: coflow injection ratio = 7·32%. ○, $x/M = 30$; △, $x/M = 40$; □, $x/M = 46$; ◇, $x/M = 60$; ⬠, $x/M = 70$.

8. Energy spectra

The one-dimensional spectrum $E_1(k_1)$, a one-dimensional projection of the wavenumber spectral density field

$$E_1(k_1) = \int_{-\infty}^{\infty}\int_{-\infty}^{\infty} e(k_1, k_2, k_3)\, dk_2 dk_3,$$

can be computed approximately† from the measured frequency spectrum $\phi_1(f)$ using the relation

$$E_1(k_1) = (\overline{U}/2\pi)\,\phi_1[f(k_1)], \tag{15}$$

where

$$k_1 = 2\pi f/\overline{U}. \tag{16}$$

Thus,

$$\overline{u^2} = \int_0^{\infty} \phi_1(f)\, df = \int_0^{\infty} E_1(k_1)\, dk_1. \tag{17}$$

All measured spectra showed a self-preserved‡ character, when properly scaled. Figure 11 is typical; $\phi_1(f)/\phi^*$ (or $E_1(k_1)/E_1^*$) is plotted versus f/f^* (or k_1/k_1^*), where $\phi^* \equiv \overline{u^2}\,\eta/\overline{U}$ has the same dimensions as $\phi_1(f)$, and $f^* \equiv \overline{U}/\eta$ has the same dimensions as f. η is the Kolmogorov microscale. Clearly we are rescaling the variables with certain length and time scales, presumably characterizing the high wavenumber fluctuations. Also, from the definitions of ϕ^* and f^*, the area under each of these spectrum functions is unity.

† The Taylor approximation; see for example Comte-Bellot & Corrsin (1971).

‡ See, for example, Stewart & Townsend (1951).

Note that the spectrum actually has a maximum, and thus does not decrease monotonically with increasing wavenumber, as it would have to for fully isotropic turbulence. The reason is that the limited size of the experiment distorts the largest eddies, and actually limits the maximum eddy size. Therefore, there must be a finite region of very small wavenumbers where $e(k_1, k_2, k_3)$ is actually zero, and hence does not contribute to the integral

$$E_1(k_1) = \int_{-\infty}^{\infty} \int_{-\infty}^{\infty} e(k_1, k_2, k_3)\, dk_2 dk_3. \tag{18}$$

It should be remarked that $E_1(0)$ is not necessarily zero, as was suggested by Comte-Bellot & Corrsin (1971). To see this, suppose that the minimum wavenumber is (k_1^*, k_2^*, k_3^*); then

$$E_1(0) = 2 \int_{k_3^*}^{\infty} \int_{k_2^*}^{\infty} e(0, k_2, k_3)\, dk_2 dk_3,$$

which is not zero in general.

By plotting the experimentally obtained one-dimensional spectrum, we were able to fair a smooth curve through the data in essentially a least-squares sense. For truly isotropic turbulence the $E_1(k)$ spectrum decreases monotonically, and behaves as k_1^2 near $k_1 = 0$ (see, for example, Corrsin 1959). We extrapolated the faired curve to $k_1 = 0$, by a downward parabola, hoping that the modified (extrapolated) spectrum corresponds to a mathematically possible flow field which is identical to the real field at moderate and large wavenumbers. This hypothetical field must have infinite duration in time and must extend to infinity in space (Comte-Bellot & Corrsin 1971).

To get the three-dimensional energy spectrum function $E(k)$, we then used the isotropic relation:†

$$E(k,t) = \tfrac{1}{2} k_1^3 \frac{\partial}{\partial k_1} \left\{ \frac{1}{k_1} \frac{\partial}{\partial k_1} E_1(k_1, t) \right\} \Bigg|_{k_1 = k}, \tag{19}$$

such that

$$\tfrac{3}{2} \overline{u^2} = \int_0^{\infty} E(k,t)\, dk.$$

Equation (19) involves double differentiation, and a Leasco time-sharing digital computer was used to perform this numerically.‡

Figure 12 shows $E(k,t)/E^*$ versus k/k^*, where $E^* \equiv (\nu^5 \epsilon)^{\frac{1}{4}}$ and $k^* \equiv \eta^{-1}$. This is 'Kolmogorov scaling'. The curves collapse for $k/k^* > 0{\cdot}01$, indicating similarity at high wavenumbers. For the low wavenumber region ($k/k^* < 0{\cdot}01$) injection seems to lower the energy, as remarked in § 7.

To examine the decay of the three-dimensional energy spectrum we plotted (figure 13) $E(k,t)$ versus k, for $J = 7{\cdot}32\ \%$ (coflow), at different downstream distances from the grid. The maxima shift slowly towards the low wavenumber region with increasing distance from the grid. On the same figure are the 'longitudinal' integral scale L_f, and the 'lateral' microscale λg. L_f^{-1} corresponds to a wavenumber slightly less than the one at the peak of each curve.

† See, for example, Hinze (1959, p. 171).

‡ Each differentiation was preceded by the appropriate curve fitting.

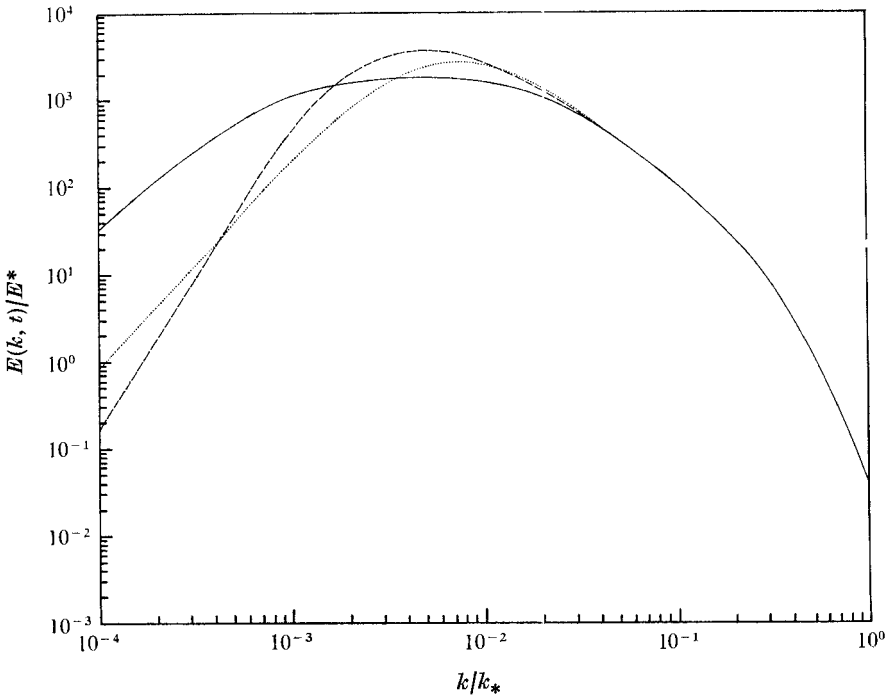

FIGURE 12. Normalized three-dimensional energy spectra: $x/M = 46$; $R_M = 4{\cdot}83 \times 10^4$. ———, $J = 0$; ·····, $J = 7{\cdot}32\%$ (coflow); – – – –, $J = 7{\cdot}32\%$ (counterflow).

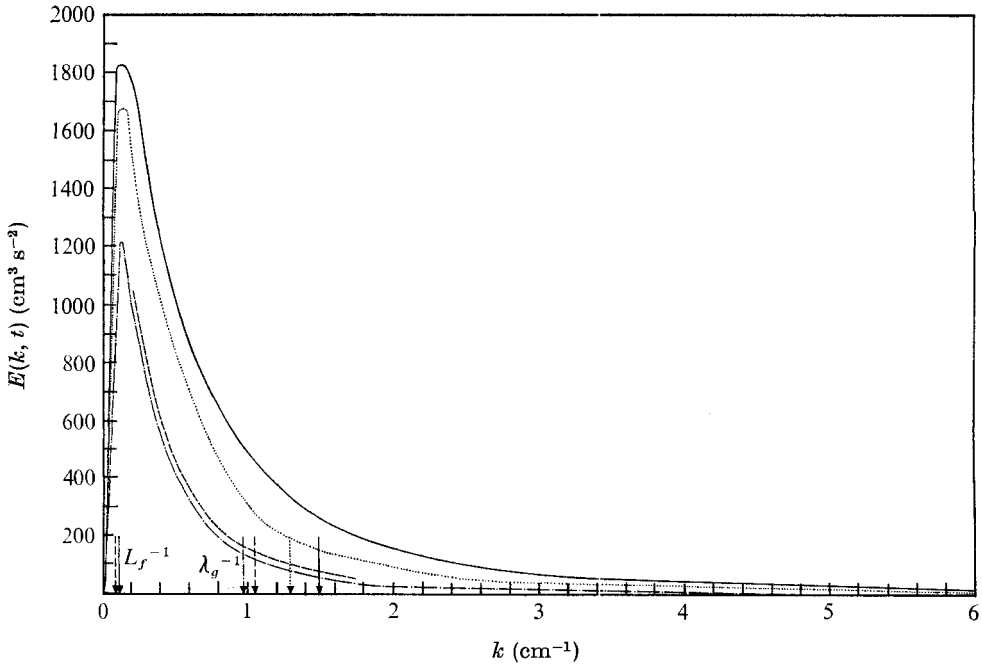

FIGURE 13. Decay of three-dimensional energy spectrum function: $J = 7{\cdot}32\%$ (coflow). ———, $x/M = 30$; ·····, $x/M = 40$; – – – –, $x/M = 60$; –·–·–·–, $x/M = 70$.

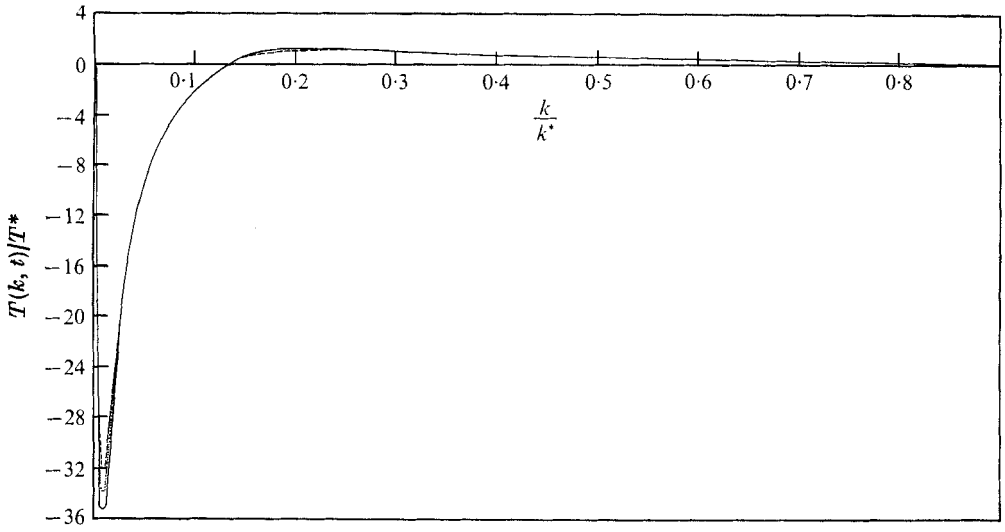

FIGURE 14. Normalized spectral transfer function: $J = 7{\cdot}32\%$ (coflow).
———, $x/M = 40$; ·····, $x/M = 50$; – – – –, $x/M = 60$.

From $E(k,t)$, we were able to compute a spectral transfer function $T(k,t)$ by using the isotropic relation

$$\partial E(k,t)/\partial t = T(k,t) - 2\nu k^2 E(k,t). \tag{20}$$

After plotting $E(k, x/\overline{U})$ at different x/M, we plotted $E(k, x/\overline{U})$ at fixed k, as a function of x/M. Then we faired a curve through the data points, taking care that the curves (for different k's) constitute a 'family'. From each of these 100 curves we read 50 data points for $E(x/M)$ at fixed k, and fed them to the differentiation subroutine to get $\partial E/\partial X$, $\partial E/\partial t$† and thus $T(k,t)$.

Figure 14 shows $T(k,t)/T^*$ versus k/k^* [$T^* \equiv (\nu\epsilon)^{\frac{1}{4}}$], for $J = 7{\cdot}32\,\%$ (coflow), at different downstream distances from the grid. To see the positive and the negative parts of the curves more clearly, each is amplified in figure 15.

Figure 16 shows $T(k,t)$ versus k for the runs shown in figure 14. As expected‡

$$\int_0^k T(k',t)\,dk'$$

at any finite k decreases with increasing distance from the grid.

In principle, the spectral transfer function must satisfy

$$\int_0^\infty T(k,t)\,dk = 0.$$

Clearly our data do not fulfill this requirement. In all runs the negative area is larger than the positive one, by as much as 50 %. Uberoi (1963) observed a similar effect, although his error was only about 13 %. Van Atta & Chen (1969)

† $\partial E/\partial t \doteq \overline{U}\,\partial E/\partial x$ (Taylor's approximation).

‡ Not immediately obvious but far from the grid, the dissipation is smaller and the amount of energy transferred from one wavenumber to another is smaller.

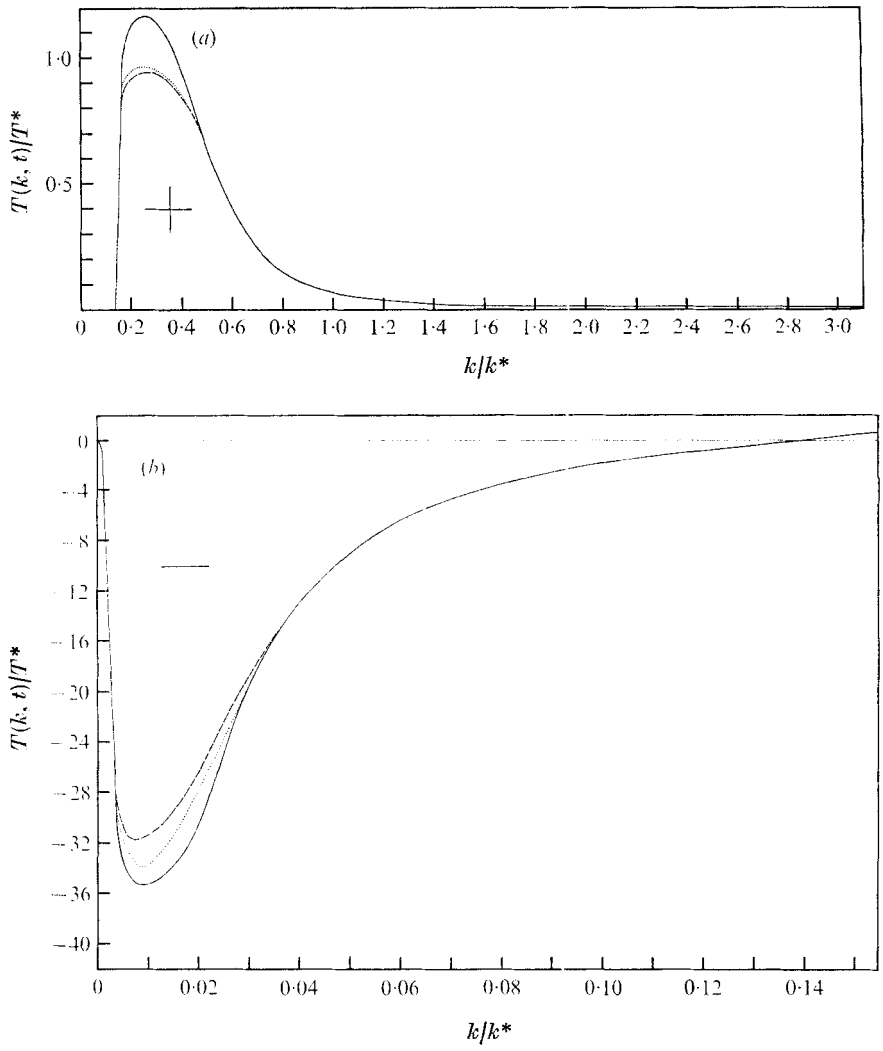

FIGURE 15. Details of figure 14.

discussed the inapplicability of equation (20) in the (necessarily anisotropic) low wavenumber region. More recently Comte-Bellot (private communication) and her colleagues at l'Ecole Centrale de Lyon computed the transfer function for some standard grid-turbulence experiments, and found the same order of error (50 %).

It can be shown that

$$\max_{0\leqq k\leqq\infty}\left|\int_0^k T(k',t)\,dk'\right| \leqq \epsilon,$$

where ϵ is the rate of energy dissipation per unit mass. The present data do not fulfill this requirement in the small wavenumber region where $T(k,t) < 0$. There is no indication that the positive region of $T(k,t)$ has any large systematic error. At small wavenumbers $\partial E/\partial t$ is the main contributor to the calculation of T.

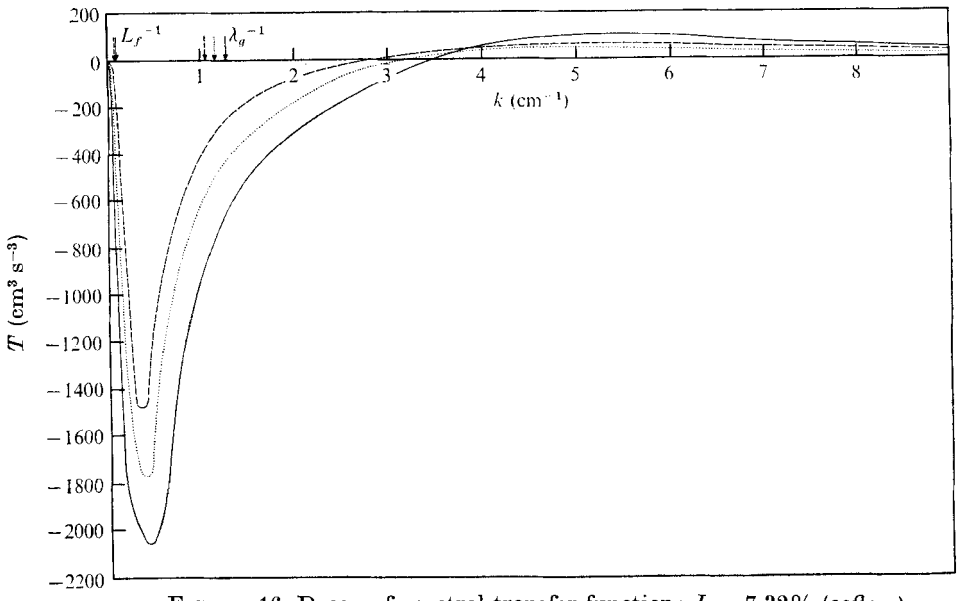

FIGURE 16. Decay of spectral transfer function: $J = 7{\cdot}32\%$ (coflow).
———, $x/M = 40$; ·····, $x/M = 50$; – – – –, $x/M = 60$.

It seems likely that our estimated values of $\partial E/\partial t$ are 'too negative' in this small wavenumber range.

The first computational remedy which comes to mind is changing the one-dimensional spectrum extrapolation to zero wavenumber. If we change the extrapolation by 3 %, $\partial E/\partial t$ changes by 15 %, not enough to account for the large error.

Reviewing our procedure, it appears that, to have

$$\int_0^\infty T\,dk$$

exactly zero, we should use the experimental data *as they are*. Any changes in the actual data change the balance between the 'positive' and the 'negative' energy transfer. An immediate difficulty is that an $E_1(k_1)$ which did not decrease monotonically would lead to the impossible result of a negative region in the three-dimensional spectrum. The reason is, of course, that we applied the isotropic relation (19) to the necessarily anisotropic low wavenumber region.

The error is evidently inherent in wind-tunnel experiments. Specifically, it may be a consequence of the non-infinite spatial and temporal sizes of all experiments.

9. Scales of turbulence

One of the important characteristic lengths of the turbulence structure is the macro- or integral scale. The longitudinal integral scale is defined as follows:

$$L_f(t) \equiv \int_0^\infty f(r, t)\,dr, \tag{21}$$

where $f(r, t)$ is the longitudinal velocity correlation coefficient.

A way to evaluate the integral scales is to extrapolate the one-dimensional energy spectrum functions to $k_1 = 0$:

$$L_f(t) = (\pi/2\overline{u^2})\, E_1(0,t) \tag{22}$$†

or, in terms of the frequency spectrum,

$$L_f(t) = (\overline{U}/4\overline{u^2})\, \phi_1(0,t). \tag{23}$$

The estimated error in determining L_f is as high as $\pm 6\ \%$ owing to some arbitrariness in the extrapolation technique.

Another important scale is the Taylor microscale. The 'lateral' microscale λ_g can be defined by

$$\frac{1}{\lambda_g^2} \equiv -\frac{1}{2}\frac{\partial^2 g(r,t)}{\partial r^2}\bigg|_{r=0}. \tag{24}$$

To evaluate λ_g, we use the following isotropic dynamic relation:

$$\frac{1}{\overline{u^2}}\frac{\partial \overline{u^2}}{\partial t} = -\frac{10\nu}{\lambda_g^2} \tag{25}$$

and, using the Taylor 'frozen pattern' approximation and a power law for decay, we get

$$\lambda_g^2 = (10\nu/n\overline{U})\,(x - x_0). \tag{26}$$

The estimated error is about $\pm 3\ \%$.

A common choice of turbulence Reynolds number is

$$R_\lambda \equiv u'\lambda_g/\nu. \tag{27}$$

The time rate of dissipation of turbulence kinetic energy into internal energy per unit mass ($\epsilon \equiv -\frac{3}{2}\, d\overline{u^2}/dt$) can be evaluated. Using the Taylor approximation and the power law for decay, we get

$$\epsilon = \frac{3}{2}\frac{\overline{U}^3 n}{BM}\left(\frac{x}{M}\right)^{-(n+1)}. \tag{28}$$

The Kolmogorov length and velocity scales are defined as follows:

$$\eta \equiv (\nu^3/\epsilon)^{\frac{1}{4}}, \quad v \equiv (\nu\epsilon)^{\frac{1}{4}}. \tag{29), (30}$$

A measure of the relative rate of decay is the non-dimensional parameter $(L_f/u'^3)\, du'^2/dt$. It can be shown that

$$C_1 \equiv \epsilon\frac{L_f}{u'^3} = -\frac{3}{2}\frac{L_f}{u'^3}\frac{du'^2}{dt} = \frac{15}{R_\lambda}\frac{L_f}{\lambda_g}. \tag{31}$$

C_1 is hopefully a numerical constant of order one.

To summarize the downstream evolution of the different scales of turbulence, we tabulated in table 3 the values of L_f, λ_g, R_λ, C_1, ϵ and η at different downstream distances from the grid.

The effects of injection on the different scales of turbulence are summarized in table 4. The counterflow injection yields larger integral and microscales than the coflow injection. The relative rate of decay C_1 is higher for the passive (no injection) case, consistent with the higher exponent of decay n.

† For derivation of this and the following equations, see books by Batchelor (1953), Hinze (1959), Monin & Yaglom (1971) and others.

Mode of operation	R_M ($\times 10^{-4}$)	J (%)	x/M	L_f (mm)	λ_g (mm)	R_λ	C_1	ϵ (cm^2/s^3)	η (mm)
Coflow injection	4·83	7·32	30	96·6	6·72	112	1·93	3101	0·32
			40	93·0	7·77	110	1·63	1684	0·38
			46	97·5	8·23	109	1·63	1303	0·40
			60	114·6	9·51	107	1·69	712	0·47
			70	111·4	10·27	106	1·53	514	0·51
Counterflow injection	4·83	7·32	30	91·1	7·01	150	1·30	4685	0·29
			40	107·0	8·11	149	1·33	2612	0·34
			46	121·6	8·53	148	1·44	2041	0·36
			60	129·5	9·91	148	1·32	1146	0·41
			70	155·1	10·70	148	1·47	838	0·45
Zero injection	4·83	0·00	30	113·4	6·16	105	2·63	3890	0·31
			40	113·4	7·12	100	2·39	1987	0·36
			46	119·2	7·47	99	2·43	1503	0·39
			60	130·1	8·72	94	2·38	771	0·46
			70	134·1	9·42	91	2·35	538	0·50

TABLE 3. Downstream evolution of scales

Mode of operation	x/M	R_M ($\times 10^{-4}$)	J (%)	L_f (mm)	λ_g (mm)	R_λ	C_1	ϵ (cm^2/s^3)	η (mm)
Coflow injection	46	7·34	4·70	84·7	6·36	109	1·86	3780	0·31
		6·50	5·34	83·8	6·86	107	1·71	2610	0·34
		6·26	5·56	86·9	6·96	105	1·78	2354	0·35
		5·72	6·12	92·7	7·41	105	1·79	1831	0·37
		4·83	7·32	97·5	8·23	109	1·63	1303	0·40
		4·18	8·55	107·6	9·07	120	1·49	1054	0·43
Counterflow injection	46	7·34	4·70	105·2	6·89	156	1·47	5425	0·28
		6·50	5·34	103·9	7·01	141	1·58	4208	0·30
		6·26	5·56	101·8	7·01	141	1·54	3902	0·31
		5·72	6·12	110·0	7·47	140	1·58	3115	0·33
		4·83	7·32	121·6	8·53	148	1·44	2041	0·36
		4·18	8·55	134·7	9·45	160	1·34	1558	0·39
Zero injection	46	7·34	0·00	110·3	6·28	130	2·02	5791	0·28
		6·50	0·00	97·8	6·64	123	1·80	3874	0·31
		6·26	0·00	121·3	6·76	118	2·28	3404	0·32
		5·72	0·00	129·2	6·98	108	2·57	2464	0·35
		4·83	0·00	119·2	7·47	99	2·43	1503	0·39

TABLE 4. Effects of injection on scales

10. Concluding remarks

A jet grid has been used to generate a field of nearly homogeneous and nearly isotropic turbulence in a wind tunnel. The jet grid was operated in three modes: coflow injection, counterflow injection and zero injection.

The lateral homogeneity attained far from the jet grid ($x/M \geqslant 30$) is within 'acceptable' limits. Homogeneity improvement over prior related experiments was attained by the use of controllable nozzles. The mean velocity profiles are

flat within 2 %, except for the counterflow-injection mode, where the deviation is as high as 5 %.

A necessary condition for homogeneity is the smallness of the ratio of a typical production term in the turbulence kinetic energy equation to a typical dissipation term. In the present experiment this ratio is less than 0·01.

The degree of isotropy, as indicated by the degree of equality of turbulence components in the streamwise (axial) and transverse directions (e.g. $u'/v' - 1$), is found to be acceptable.

The transfer functions do not have equal positive and negative areas as they should. The error is as large as 50 %. Apparently, the error is inherent in wind-tunnel experiments owing to the spatial and temporal finiteness of these experiments.

The jet grid is a convenient configuration for studying the mixing of two gases, or of the same gas at two different temperatures.

This work was supported by the U.S. National Science Foundation, under Grant GK 10268, and the Office of Naval Research under Contract N000-14-67A-0163-0005. We should like to thank Michael Karweit and Bernard Baker for their important contributions to the experiments.

REFERENCES

Baines, W. D. & Peterson, E. G. 1951 An investigation of flow through screens. *Trans. A.S.M.E.* **73**, 467.

Batchelor, G. K. 1953 *The Theory of Homogeneous Turbulence.* Cambridge University Press.

Batchelor, G. K. & Townsend, A. A. 1947 Decay of vorticity in isotropic turbulence. *Proc. Roy. Soc.* A **190**, 534.

Batchelor, G. K. & Townsend, A. A. 1948*a* Decay of isotropic turbulence in the initial period. *Proc. Roy. Soc.* A **193**, 539.

Batchelor, G. K. & Townsend, A. A. 1948*b* Decay of turbulence in the final period. *Proc. Roy. Soc.* A **194**, 527.

Chang, P. K. 1966 *Separation of Flow.* Pergamon.

Charnay, G. 1969 Etude d'une couche limite perturbée par une turbulence extérieure. *Ecole Centrale Lyonnaise, Lab. de Mécanique des Fluides.*

Comte-Bellot, G. & Corrsin, S. 1966 The use of a contraction to improve the isotropy of grid-generated turbulence. *J. Fluid Mech.* **25**, 657.

Comte-Bellot, G. & Corrsin, S. 1971 Simple Eulerian time correlation of full and narrow band velocity signals in grid-generated isotropic turbulence. *J. Fluid Mech.* **48**, 273.

Corrsin, S. 1942 Decay of turbulence behind three similar grids. Aero. Engng thesis, California Institute of Technology.

Corrsin, S. 1944 Investigation of the behaviour of parallel two-dimensional air jets. *N.A.C.A. War-time Rep.* W-90.

Corrsin, S. 1959 Outline of some topics in homogeneous turbulent flow. *J. Geophys. Res.* **64**, 2134.

Corrsin, S. 1963 Turbulence: experimental methods. *Handbuch der Physik*, vol. 8, p. 524. Springer.

Gad-el-Hak, M. 1972 Experiments on the nearly isotropic turbulence behind a jet grid. Ph.D. thesis, Dept. Mechanics & Materials Science, The Johns Hopkins University.

GUILLON, O. 1968 Essais de mise au point d'une grille active à grandes mailles. *Ecole Centrale Lyonnaise, Lab. de Mécanique des Fluides.*

HARRIS, G. V. 1965 The turbulence generated by an array of parallel rods. M.S. thesis, The Johns Hopkins University.

HINZE, J. O. 1959 *Turbulence.* McGraw-Hill.

HOERNER, S. F. 1965 *Fluid-Dynamic Drag.* Published by the author, U.S.A.

KARWEIT, M. J. & CORRSIN, S. 1969 Fluid line growth in grid-generated isotropic turbulence. *J. Fluid Mech.* **39**, 87.

KISTLER, A. L. & VREBALOVICH, T. 1961 Turbulence measurements at the 8 by 10-foot Cooperative Wind Tunnel. *Jet Prop. Lab. Res. Summ.* no. 36-4, p. 12.

LING, S. C. & WAN, C. H. 1972 Decay of isotropic turbulence generated by a mechanically agitated grid. *Phys. Fluids*, **15**, 1363.

LIU, J. C. H., GREBER, I. & WISKIND, H. K. 1971 Experimental measurements of grid-injection turbulent flows. *Case Western Reserve University Tech. Rep.* FTAS/TR-70-53.

LUXENBERG, D. S. & WISKIND, K. 1969 Some effects of air injection on the turbulence generated by a bi-planar grid. *Case Western Reserve University Tech. Rep.* FTAS/TR-69-42.

MATHIEU, J. & ALCARAZ, E. 1965 Réalisation d'une soufflerie à haut niveau de turbulence. *Comptes Rendus*, **261**, 2435.

MONIN, A. S. & YAGLOM, A. M. 1971 *Statistical Fluid Mechanics: The Mechanics of Turbulence*, vol. 1 (English trans.). M.I.T. Press.

NAUDASCHER, E. 1965 Flow in the wake of self-propelled bodies and related sources of turbulence. *J. Fluid Mech.* **22**, 625.

NAUDASCHER, E. & FARELL, C. 1970 Unified analysis of grid turbulence. *J. Eng. Mech. Div., Proc. A.S.C.E.*, EM **2**, 121.

PRANDTL, L. & TIETJENS, O. 1934 *Fundamentals of Hydro- and Aero-mechanics.* McGraw-Hill.

ROUSE, H. 1956 Seven exploratory studies in hydraulics. *J. Hyd. Div., Proc. A.S.C.E.*, no. 1038.

SIMMONS, L. F. G. & SALTER, C. 1934 Experimental investigation and analysis of the velocity variations in turbulent flow. *Proc. Roy. Soc.* A **145**, 212.

STEWART, R. W. & TOWNSEND, A. A. 1951 Similarity and self-preservation in isotropic-turbulence. *Phil. Trans.* A **243**, 359.

TENNEKES, H. & LUMLEY, J. L. 1972 *A First Course in Turbulence.* M.I.T. Press.

TEUNISSEN, H. W. 1969 An ejector-driven wind tunnel for the generation of turbulent flows with arbitrary mean velocity profile. *UTIAS Tech. Note, University of Toronto*, no. 133.

TSUJI, H. 1955 Experimental studies on the characteristics of isotropic turbulence behind two grids. *J. Phys. Soc. Japan*, **10**, 578.

TSUJI, H. & HAMA, F. R. 1953 Experiment on the decay of turbulence behind two grids. *J. Aero. Sci.* **20**, 848.

UBEROI, M. S. 1963 Energy transfer in isotropic turbulence. *Phys. Fluids*, **6**, 1048.

VAN ATTA, C. W. & CHEN, W. Y. 1969 Measurements of spectral energy transfer in grid turbulence. *J. Fluid Mech.* **38**, 743.

VON BOHL, J. G. 1940 Das Verhalten paralleler Luftstrahlen. *Ing.-Arch.* **11**, 295.

WYATT, L. A. 1955 Energy and spectra in decaying homogeneous turbulence. Ph.D. thesis, University of Manchester.

WYNGAARD, J. C. 1968 Measurement of small-scale turbulence structure with hot wires. *J. Sci. Instrum.* **1** (2), 1105.

WYNGAARD, J. C. 1969 Spatial resolution of the vorticity meter and other hot-wire arrays *J. Sci. Instrum.* **2** (2), 983.

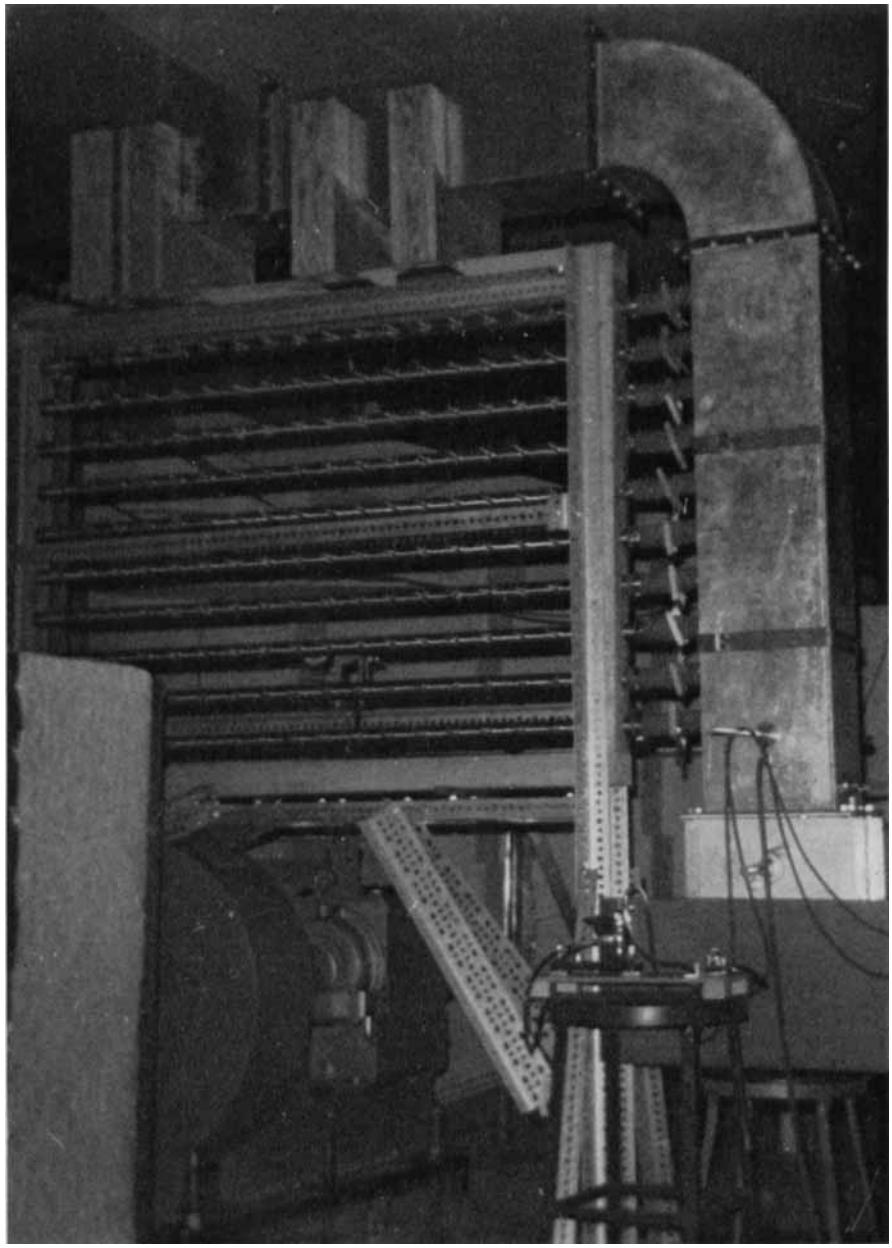

FIGURE 1. The jet grid and secondary air blower.

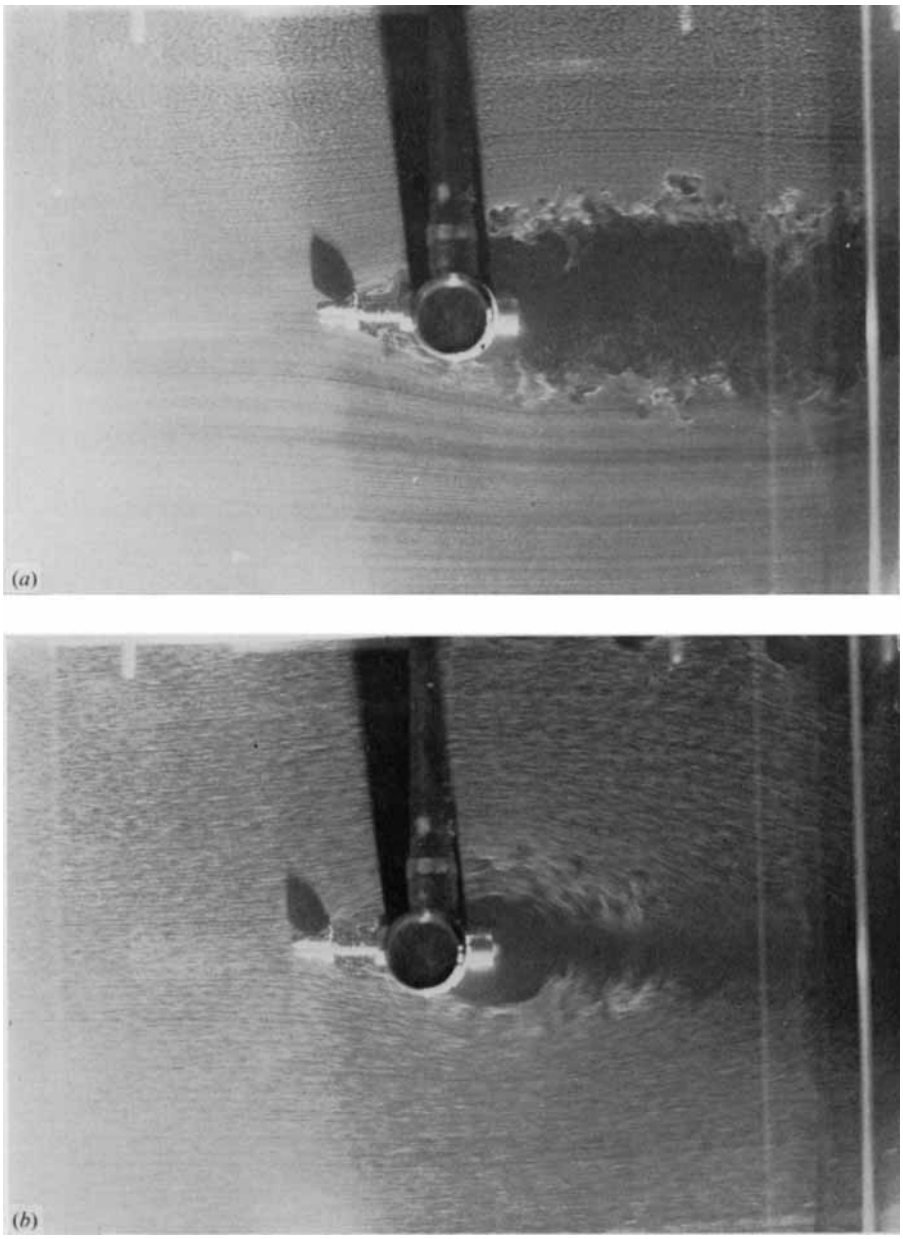

FIGURE 2. Hydrogen-bubble pictures, jet directed downstream.
(*a*) No injection, $R_D \cong 10^3$. (*b*) With 5% injection ratio, $R_D \cong 10^3$.

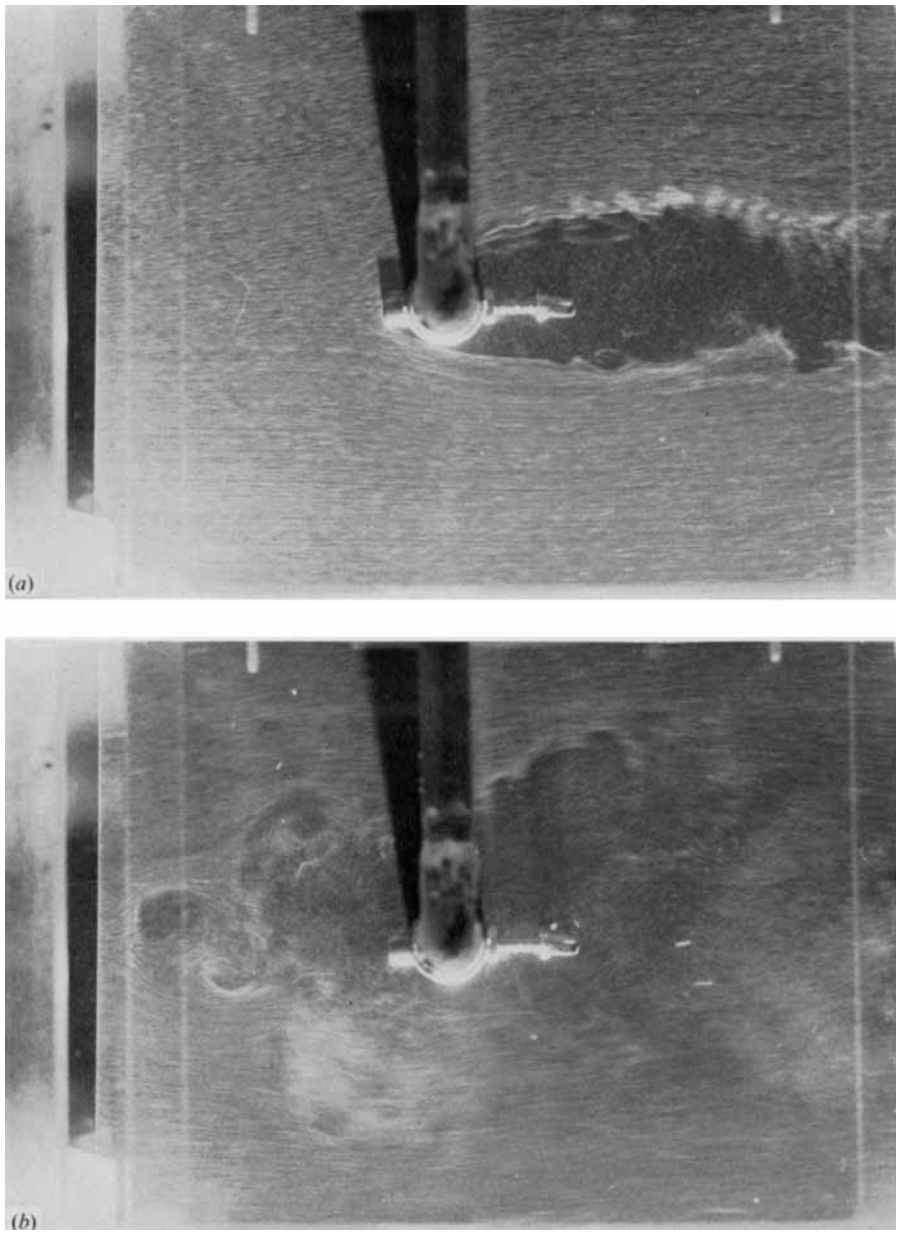

FIGURE 3. Hydrogen-bubble pictures, jet directed upstream.
(*a*) No injection, $R_D \cong 10^3$. (*b*) With 5% injection ratio, $R_D \cong 10^3$.